Gyrokinetic turbulence under near-separatrix or nonaxisymmetric conditions[a)]

F. Jenko,[1,b)] D. Told,[1] P. Xanthopoulos,[2] F. Merz,[1] and L. D. Horton[1]
[1]*Max-Planck-Institut für Plasmaphysik, Boltzmannstr. 2, D-85748 Garching, Germany*
[2]*Max-Planck-Institut für Plasmaphysik, Teilinstitut Greifswald, Wendelsteinstr. 1, D-17491 Greifswald, Germany*

(Received 5 December 2008; accepted 6 January 2009; published online 19 March 2009)

Linear and nonlinear gyrokinetic simulations with the GENE code [F. Jenko *et al.*, Phys. Plasmas **7**, 1904 (2000)] for tokamak edge plasmas as well as for stellarator core plasmas are presented, shedding light on the behavior of plasma microturbulence under near-separatrix or nonaxisymmetric conditions. To this aim, the required geometric coefficients are inferred directly from the magnetohydrodynamic equilibria of three different devices via the newly developed GIST code. It is found that the residual electron heat transport level in the *H*-mode edge can be explained in terms of high-wave-number fluctuations driven by electron temperature gradient modes. Moreover, the study of adiabatic ion temperature gradient turbulence in optimized stellarators points to the possibility of a systematic geometric optimization with respect to anomalous transport in nonaxisymmetric devices. © *2009 American Institute of Physics*. [DOI: 10.1063/1.3089603]

I. INTRODUCTION

As is well known, turbulent transport in fusion plasmas is driven by microinstabilities whose linear and nonlinear properties may depend significantly on the magnetic geometry of the respective device, discharge, and radial location. However, since the vast majority of gyrokinetic turbulence simulations found in literature deals with typical tokamak core conditions, the geometric coefficients for these investigations are often simply taken from the $\hat{s}$-α model for circular, large aspect ratio tokamaks.[1] Sometimes, a Miller model equilibrium[2] is used instead, increasing the (geometric) realism substantially. However, as one approaches the separatrix, this model breaks down at some point, since it cannot capture the complexities of extreme shaping and strong up-down asymmetry. Thus, it becomes necessary to infer the required geometric coefficients directly from magnetohydrodynamic (MHD) equilibria. This is even truer of nonaxisymmetric devices which are, in general, very hard to model, although such attempts have been made.[3]

In the present work, we shall be interested in the properties of gyrokinetic turbulence under near-separatrix or nonaxisymmetric conditions. Employing the gyrokinetic turbulence code GENE,[4–6] we will study the linear and nonlinear behavior of various microinstabilities in ASDEX Upgrade (Axially Symmetric Divertor Experiment) (Ref. 7) edge plasmas as well as in NCSX (National Compact Stellarator Experiment) (Ref. 8), and Wendelstein 7-X (Ref. 9) core plasmas. In this context, it will become clear that despite certain similarities between these cases and more standard tokamak core scenarios, there are also important differences. For example, in a tokamak edge, electron temperature gradient (ETG) modes may have poloidal wavelengths of a few *ion* gyroradii (but radial wavelengths still of the order of an electron gyroradius), and they may peak well away from the outboard midplane—even close to the *X*-point(s) of the plasma. In nonlinear simulations, we will find that the residual electron heat transport level in the *H*-mode (high confinement mode) edge (at least for a particular ASDEX Upgrade discharge) can be explained in terms of high-wave-number fluctuations driven by ETG modes. Moreover, adiabatic ion temperature gradient (ITG) turbulence simulations for the core of optimized stellarators such as Wendelstein 7-X or NCSX suggest that there might actually be the possibility of a systematic geometric optimization with respect to anomalous transport in nonaxisymmetric devices which should be explored in more detail in the future.

The numerical tools used in the present study are the gyrokinetic turbulence code GENE (Refs. 4–6) and the geometry interface GIST (see Sec. III A). GENE solves the nonlinear gyrokinetic equations on a fixed grid in phase space. It can deal with an arbitrary number of fully gyrokinetic particle species (passing and trapped), electromagnetic effects, collisions (including both pitch angle and energy scattering between like and unlike particles), and sub-ion-gyroradius physics (including finite Debye length effects). In the linear regime, GENE can also be used as an eigenvalue solver, so that subdominant microinstabilities can be tracked.[10] While GENE has recently been extended to include nonlocal effects in the radial direction, such that it can also be run as a global code, all the simulation results in this paper were obtained in the local mode of operation.

As mentioned before, the main goal of the present work is to explore the linear and nonlinear behavior of various microinstabilities under extreme geometric conditions as they occur in the edge region of tokamaks and in stellarators. Now, for efficiency reasons, GENE employs field-aligned coordinates, and the required metric coefficients are obtained directly from MHD equilibria[11] the newly developed GIST code. Thus, there are no approximations or special assump-

[a)]Paper NI1 6, Bull. Am. Phys. Soc. **53**, 160 (2008).
[b)]Invited speaker.

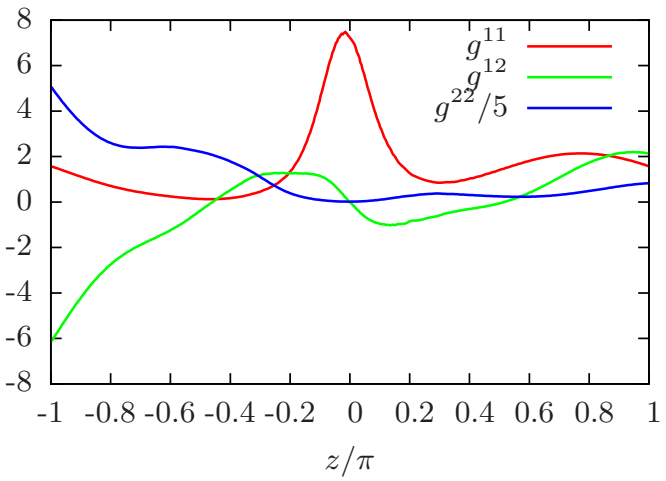

FIG. 1. (Color online) Metric coefficients for the $\varrho_{\mathrm{pol}}=0.98$ flux surface of ASDEX upgrade shot 20431 during its low power phase.

tions being made in order to simplify or model the geometric input data. Instead, we work with the full geometric information contained in the experimental MHD files. This allows us, in particular, to perform very accurate simulations in the neighborhood of the separatrix, where the influence of the *X*-point is clearly reflected in the behavior of the metric coefficients, and in devices with a high level of nonaxisymmetry.

The remainder of this paper is organized as follows. In Sec. II, GENE results for a particular ASDEX Upgrade edge plasma will be presented. In this context, the linear and nonlinear properties of edge ETG modes will be the main focus. It will be shown that these modes are able to explain the residual electron heat transport in the *H*-mode edge. In Sec. III, we will show GENE simulations for the optimized stellarators Wendelstein 7-X and NCSX, concentrating on the properties of adiabatic ITG turbulence in these devices. From these results, we will be able to conclude that there seems to exist a significant potential for a systematic optimization of turbulent transport due to nonaxisymmetric shaping. In Sec. IV, we will provide a brief summary and some conclusions.

II. GYROKINETIC TURBULENCE IN TOKAMAK EDGE PLASMAS

As pointed out in Ref. 12, simulations for the plasma edge have primarily been done in simplified model geometries and/or with simplified physics models so far. The present work is intended to extend these previous studies to quite comprehensive (local) gyrokinetic simulations for a particular ASDEX Upgrade discharge. In this context, we will be particularly interested in the question which modes are likely to set the residual electron heat transport level in the steep gradient zone of an *H*-mode plasma—leaving the mechanisms underlying the *L*-*H* transition itself for future studies.

A. Some background on the physical and numerical parameters

For the purposes of the present study, we will employ the plasma parameters and geometrical information from the ASDEX Upgrade shot No. 20431 at $t=1.82$ s. This discharge had a toroidal current of 1.0 MA and a toroidal magnetic field of 2.4 T. At the point in time analyzed in this paper, there was 5.0 MW of neutral beam injection and 2.5 MW of ion cyclotron (H minority) heating. At this heating level and with a line averaged density of 4.6×10^{19} m^{-3}, the input power was a factor of 7 above the *H*-mode power threshold, and the discharge had clear type I ELMs with a confinement enhancement factor of 1.1. Therefore, this case is to be considered as an example of a discharge that is deep in the *H*-mode regime. We would like to note in passing that the MHD equilibrium has been calculated taking into account the large pressure gradients in the edge. This treatment leads to a kinked q profile near the edge, corresponding to a slight shear reversal (see also Ref. 12). For the simulations shown here, we choose the flux surface $\varrho_{\mathrm{pol}}=0.98$, situated within the steep gradient zone. In Fig. 1 the metric coefficients g^{11}, g^{12}, and g^{22}—obtained using GIST—are shown. The influence of the nearby separatrix is reflected in the comparatively large range of values these coefficients can take.

The temperature and density profiles are obtained through hyperbolic tangent fits[13] to the data from various plasma diagnostics, averaged over the time window $t=1.65-2.0$ s. Table I shows our nominal input parameters, the gradients being defined according to the formula

$$\omega_x = -\frac{1}{x}\frac{dx}{d\varrho_{\mathrm{tor}}}.$$

Here, x represents the temperatures T_e and T_i, or the particle density n, while $\varrho_{\mathrm{tor}}=\sqrt{\Phi/\Phi_{\mathrm{edge}}}$ and Φ is the toroidal flux. For labeling the flux surfaces in the present paper, we use $\varrho_{\mathrm{pol}}=\sqrt{\Psi/\Psi_{\mathrm{edge}}}$ with the poloidal flux Ψ. All frequencies are given in units of $c_s/L_\perp$, where c_s is the ion sound speed and $L_\perp=\sqrt{\Phi_{\mathrm{edge}}/\pi B_0}$; B_0 is the magnetic field on the magnetic axis. Using this definition, we get $L_\perp=0.669$ m, which corresponds roughly to the average minor radius. In this context, we would like to point out that the experimental uncertainties for the T_i profile are larger than those for the T_e and n profiles. This is due to the fact that there was no edge ion temperature diagnostics available. Thus, there are only few data points to determine the fit we use. For the electron tempera-

TABLE I. Plasma parameters for the $\varrho_{\mathrm{pol}}=0.98$ flux surface of ASDEX upgrade shot 20431 during its low power phase. The values are slightly different from those in Ref. 12 since an updated set of parameters was used.

ω_{Ti}	ω_{Te}	ω_n	T_e (keV)	n_e (m^{-3})	T_i/T_e	q	$\hat{s}$	m_i/m_e	c_s (m/s)	ν_{ei} (kHz)	β_e (%)
14.3	24.8	11.2	0.69	3.0×10^{19}	1.93	4.6	0.84	3670	1.82×10^5	551	0.16

ture and density, the measurements were taken prior to an ELM, whereas for the ion temperature there is no ELM synchronizing.

Linear simulations with GENE for these plasma conditions have been carried out with 32×16 grid points in $(v_\parallel,\mu)$ velocity space, using at least 64 grid points in the parallel direction and 12 k_x values (allowing for parallel connections across the box boundary), while probing only a single k_y mode at a time. Here, the perpendicular box size was determined by the expressions $L_y=2\pi/k_y$ and $L_x=1/(\hat{s}k_y)$ where $\hat{s}$ is the (global) magnetic shear of the flux surface under consideration. The convergence of the results under these conditions was checked by means of careful resolution tests. For nonlinear simulations, on the other hand, the phase space grid was comprised of 96 points in radial and binormal directions, whereas the parallel resolution was decreased to 32 points. The $(v_\parallel,\mu)$ velocity space was discretized (in the standard runs) by 24×8 points. The following resolution tests were performed to show the adequacy of these values in terms of physical results:

- Velocity space resolution was increased to 32 and 16 points in the $v_\parallel$ and μ direction, respectively.
- Parallel resolution was tested up to 256 points.
- Perpendicular resolution was doubled compared to the standard values.

Although the transport values were observed to vary by up to a factor of about 2, the results did not change qualitatively.

B. Linear simulation results

As has been shown in Ref. 12, in the very long-wavelength regime of the linear growth rate spectrum, one finds ITG modes at $0.01\lesssim k_y\varrho_s\lesssim0.1$ with $\gamma\lesssim1.6\ c_s/L_\perp$, and microtearing modes at $0.1\lesssim k_y\varrho_s\lesssim0.2$ with $\gamma\lesssim0.16\ c_s/L_\perp$. Here, $\varrho_s=c_s/\Omega_i$ is the ion sound radius, and Ω_i is the ion gyrofrequency. While at such scales, nonlocal effects are expected to modify the properties of these microinstabilities, their growth rates are clearly exceeded by the experimentally measured (e.g., via Doppler reflectometry) $E\times B$ shearing rates, such that by means of the well-established quench rule[14] one can safely assume that they will be suppressed.

Somewhat surprisingly, the major part of the linear growth rate spectrum (at $k_y\varrho_s\gtrsim0.2$) is actually dominated by an ETG instability (see Ref. 12) which exhibits some properties that are not known from $\hat{s}$-α core[4] or edge[15] simulations. In the present case, the maximum linear growth rates are not found for modes with zero radial wavenumber, but for modes with some finite k_x value. Consequently, two-dimensional $(k_x$-$k_y)$ spectra (see Fig. 2) have to be generated to find the most unstable modes, so that considerably more effort than in core situations is required to gain a complete linear picture.

When varying the plasma parameters, one finds that—as for core ETG modes[16]—the instability can be stabilized be decreasing the electron temperature gradient, but also by increasing the density gradient. This behavior can be summarized by relating instability to the parameter $\eta_e=dT_e/dn_e$ exceeding a critical value of $\eta_{e,\mathrm{crit}}\approx1.2$. Over the past decade or so, experiments in the ASDEX Upgrade tokamak have consistently found $\eta_e\sim2$ in the H-mode edge,[17] clearly within the unstable regime of the ETG instability discussed here. Thus, the present results indicate that it should be considered a serious candidate for setting the residual electron heat flux in the H-mode edge, which has been shown (see, e.g., Ref. 18) to be anomalous in nature. The nonlinear simulation results presented below will confirm this point of view, but first, we would like to make a few more comments concerning the unusual linear properties of these edge ETG instabilities.

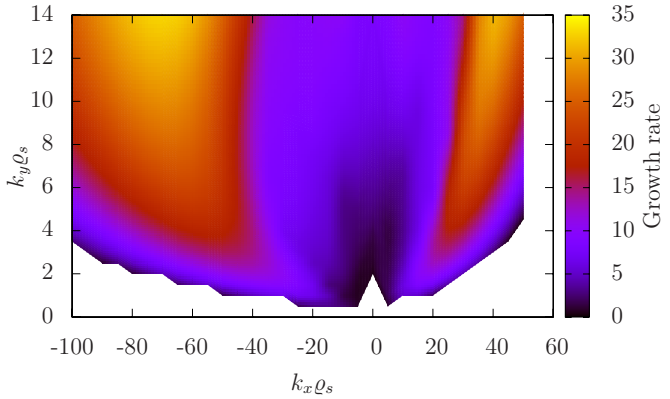

FIG. 2. (Color online) Two-dimensional growth rate spectrum (in units of $c_s/L_\perp$) in the ASDEX upgrade H-mode edge for shot 20431. The largest growth rates are obtained for finite radial wavenumbers.

One characteristic of modes with finite radial wavenumber is their peculiar behavior in the parallel direction. One finds that the largest amplitudes are reached off the outboard midplane, where they would be found in the case $k_x=0$. This behavior can be understood via an analysis of the magnetic field topology in the edge, more precisely of local shear. In the GENE setup, this quantity reads (ϕ is the cylindrical toroidal angle)[19]

$$\hat{s}_{\mathrm{loc}}=q_0\frac{d}{d\phi}\left(\frac{g^{12}}{g^{11}}\right).$$

Performing a flux tube average of this quantity, one obtains the global shear value, which is defined here as

$$\hat{s}=\frac{\varrho_{\mathrm{tor}}}{q}\frac{dq}{d\varrho_{\mathrm{tor}}}.$$

In Fig. 3, the absolute value of local shear is shown as obtained with the GIST code. Having taken the absolute value, changes in sign become visible as dark lines. Each area enclosed by such a curve is an area of negative local shear; note that this is the case for a large part of the low field side plasma, especially in the edge region. If one starts at the outboard midplane with horizontal streamers (corresponding to $k_x=0$ as in the core), negative shear tends to tilt these streamers away from the horizontal direction, leading to lower growth rates (see, e.g., Ref. 20). The effect of local shear on the x axis of the simulation box—and thus also the streamers—is illustrated in Fig. 4. On the other hand, if one

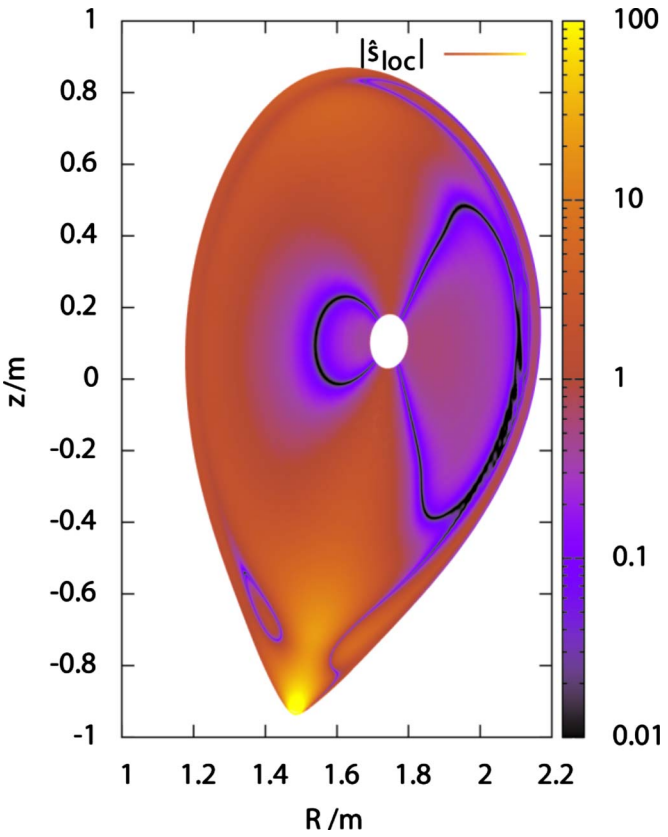

FIG. 3. (Color online) Absolute value of local shear $\hat{s}_{\mathrm{loc}}$. Changes in sign are visible as dark lines.

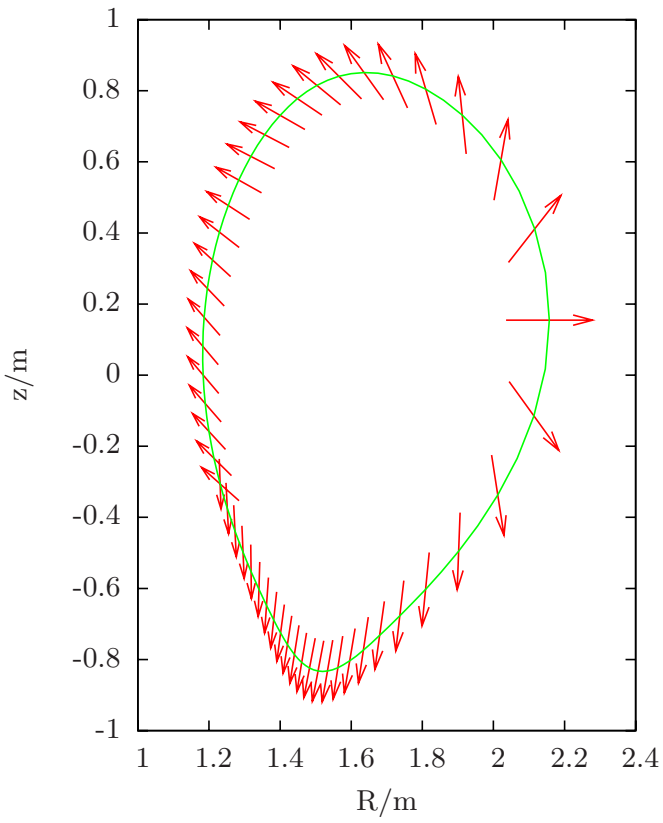

FIG. 4. (Color online) Tilting of radial structures due to negative magnetic shear.

starts with tilted streamers (corresponding to finite k_x), one can see that they become horizontal at some position away from the outboard midplane. In the most extreme case, such a mode can peak even at the top or the bottom of the plasma, which happens when $k_x \gg k_y$.

C. Nonlinear edge ETG simulations

When analyzing the linear simulations, one finds that while the most unstable modes have finite k_x values, they are very localized in the parallel direction. This fact is taken advantage of when setting up the nonlinear grid for the simulation. If the mode under consideration had a large parallel extension, one would have to use a very fine radial resolution to take into account the tilting of the mode structures by magnetic shear. Here, however, the strong localization of the instability allows for a radial grid with relatively few points. The radial extension of the simulation domain was chosen to be 1.45 ion gyroradii—measured at the outboard midplane. When following the field line, this value adapts according to the distance between the flux surfaces. As the flux surfaces are closest at the outboard midplane, the value given above is the minimal extension. With 96 radial points, the resolution at this position is 0.015 ion gyroradii.

In the nonlinear simulations, a quasistationary turbulent state is reached after about $3\,L_\perp/c_s$. Surprisingly, when examining the heat flux properties of the ETG instability one finds that, in contrast to the linear growth rates, the electron heat flux exhibits a strong peak at the outboard midplane (see Fig. 5). In accordance with the above statements, this is expected to be linked to the radial wavenumber spectra. In fact, Fig. 6 shows that the electron heat flux peaks at $k_x=0$, while in the binormal (y) direction it is localized at very small scales of $k_y\varrho_s \sim 50$. Taking into account the metrics at the outboard side, this corresponds to a physical wavenumber of $k_\perp \varrho_s \sim 15$. The radial correlation length of the structures found in the electrostatic potential is approximately one-tenth of the box size, corresponding to a 2% decrease in the

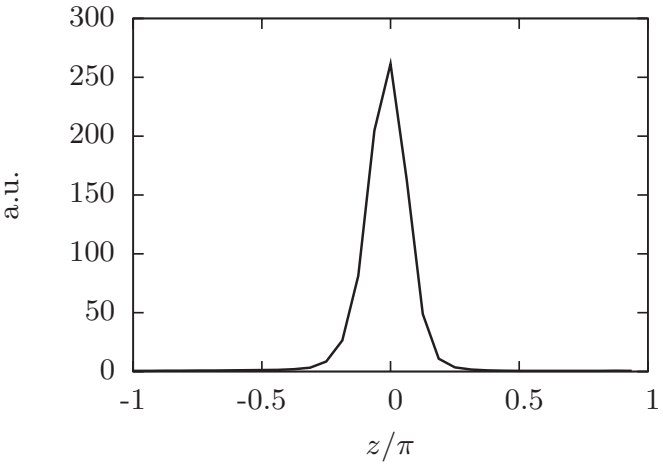

FIG. 5. Parallel profile of the ETG-induced (electrostatic) electron heat flux Q^e_{es}.

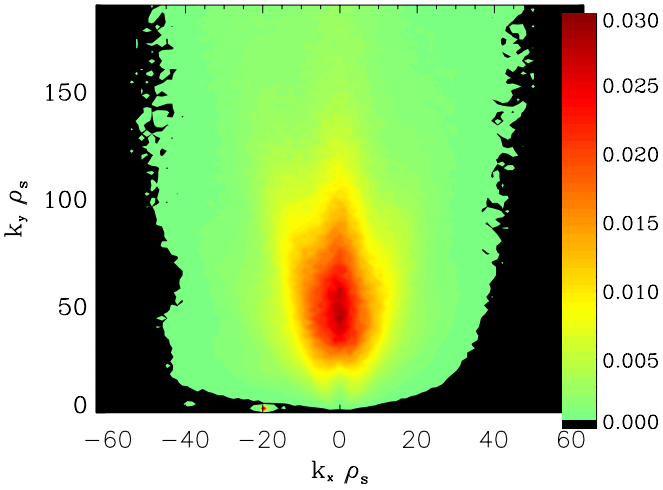

FIG. 6. (Color online) Two-dimensional wavenumber spectrum of the ETG-induced (electrostatic) electron heat flux Q^e_{es}. In contrast to the linear growth rates, the transport peaks around $k_x=0$.

background electron temperature, so that the local approximation is well justified for these high-wave-number fluctuations.

The electron heat diffusivity calculated from this simulation amounts to $\chi_e=0.83\ \mathrm{m}^2/\mathrm{s}$, which agrees quite favorably with the experimental value from an ASDEX Upgrade shot close to the *L-H* transition ($\chi_e\sim 0.4\ \mathrm{m}^2/\mathrm{s}$, see Ref. 18). Using the standard grid resolution, a scan in the electron temperature gradient (Fig. 7) reveals that the nonlinear threshold coincides well with the linear one, $\eta_{e,\mathrm{crit}}\approx 1.2$. Experimentally relevant electron heat flux levels are obtained for $\eta_e\gtrsim 1.5$. Such η_e values are in line with the experimental values, as pointed out above. Thus, ETG-induced turbulence is a main candidate for explaining the residual electron heat transport in the *H*-mode edge of tokamaks.

III. GYROKINETIC TURBULENCE IN OPTIMIZED STELLARATORS

A second class of situations in which the magnetic geometry differs strongly from the usual tokamak core conditions is that of nonaxisymmetric devices. Here, three-dimensional (3D) shaping can be exploited to modify the properties of various microinstabilities. While there already exists a multitude of publications on linear gyrokinetic simulations for various stellarators, there are only very few studies of gyrokinetic turbulence for such experiments. ETG turbulence in the Wendelstein 7-AS stellarator has been studied in Refs. 21 and 22, and ITG turbulence with adiabatic electrons for Wendelstein 7-X and the large helical device in Refs. 23 and 24, respectively. The present work aims at extending these previous investigations, focusing on the optimized stellarators Wendelstein 7-X and NCSX. In this paper, we will restrict to ITG turbulence with adiabatic electrons, although we have already performed kinetic electron simulations. The discussion of the latter will be deferred to a separate publication.

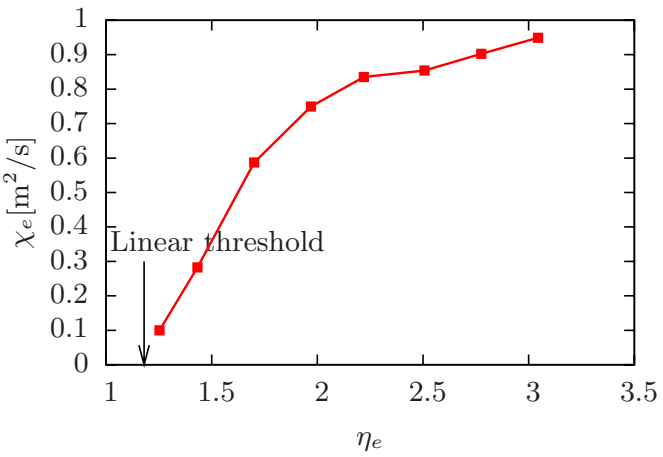

FIG. 7. (Color online) Electron heat diffusivity for different electron temperature gradients. The obtained diffusivities are of the order of the experimentally measured values.

A. The GIST code package

The nonaxisymmetry of stellarators imposes an increased complexity on the deduction of the geometric elements from MHD equilibria. The field-line tracing technique employed in the tokamak studies is restricted to flux tubes starting in the symmetry plane of the magnetic topology. This constitutes a potential drawback in the context of stellarators, since flux tubes on the same magnetic surface are expected to manifest different linear and/or nonlinear properties. At the same time, the information gathered from the field-line tracing can be useful, e.g., the cylindrical toroidal angle can be used as a convenient field-following coordinate.

In view of this, it was necessary to create an integrated package which combines the benefits of the tracing with the possibility to construct a flux tube starting at an arbitrary point of the 3D configuration. The additional modules are the codes TERPSICHORE (Ref. 25) and VVBAL,[26] which calculate the Boozer components of MHD quantities for the global equilibrium and, on this basis, the required geometric elements for the gyrokinetic simulations are reconstructed along a preselected field line. The outcome of this endeavor is the newly developed code package termed GIST (Geometry Interface for Stellarators and Tokamaks), a detailed documentation of which will appear in a forthcoming paper.

GIST reads in standard output files from VMEC equilibria[27] or the equivalent Boozer file [produced, e.g., by the JMC code (see Ref. 28)] and generates the magnetic coordinate system

$$\{x^1,x^2,x^3\}=\{\sqrt{s},\Psi_N'(x^1)[q(x^1)(\theta-\theta_k)],\phi/q\}. \tag{1}$$

Here, $s=\Phi/\Phi_{\mathrm{edge}}$ is the normalized toroidal flux, $\Psi_N=\Psi/(a^2B_a)$ is the normalized poloidal flux (a is the average minor radius, and $B_a=2\Phi_{\mathrm{edge}}/a^2$ is the normalizing magnetic field), θ is the Boozer poloidal angle, θ_k is the "ballooning angle," ϕ is the cylindrical toroidal angle, and q is the safety factor. Thus, the interface for GENE comprises the following quantities along the flux tube: The matrix of contravariant metric elements, the two curvature components entering the gyrokinetic Vlasov equation ("bad curvature" and geodesic curvature), as well as the modulus of the magnetic field and its derivative in the parallel direction.

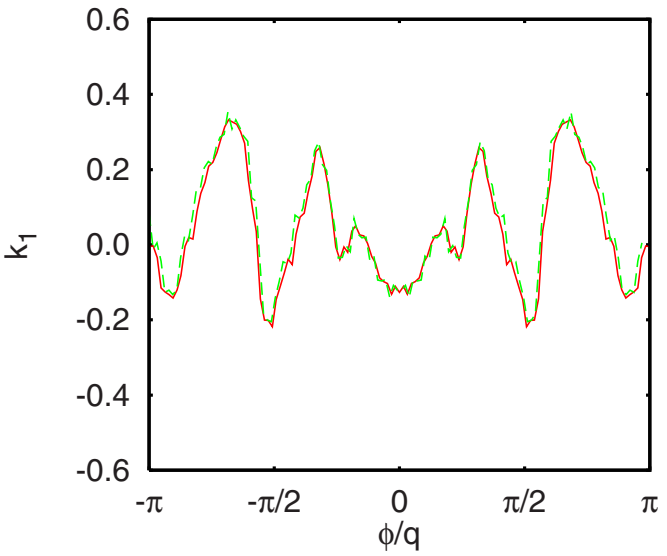

FIG. 8. (Color online) Numerical determination of the bad curvature component k_1 via field-line tracing (solid line) and an MHD approach (dashed line), validating the GIST code.

Finally, we would like to provide a consistency check, namely the calculation of the bad curvature component k_1, which is responsible for driving the microinstabilities. This term is a combination of the normal and geodesic curvatures and may be approached in two different ways:

(1) Using the MHD quantities (P=pressure, $\boldsymbol{j}$=current density, $\sqrt{g}$=Jacobian of Boozer coordinates, J=toroidal current flux, I=poloidal current flux; the prime denotes a derivative with respect to s)

$$k_1 = -\frac{a^2\sqrt{s}B_a}{qB}\left\{\frac{q'(s)B}{2P'}\boldsymbol{B}\cdot\boldsymbol{\nabla}\left(\frac{\boldsymbol{j}\cdot\boldsymbol{B}}{B^2}\right)(\theta-\theta_k) - \frac{B}{2\sqrt{g}\Psi'} \times\left[\sqrt{g}\boldsymbol{B}\cdot\boldsymbol{\nabla}(B_s/B^2) + \frac{\sqrt{g}P'}{B^2} + \frac{1}{B^2}(J\Psi'' - I\Phi'') - \partial_s\sqrt{g}\right]\right\}. \quad (2)$$

(2) Using the field-line orbit projected on the surface geometry (r, z=cylindrical coordinates, C_2^1=projection of $\boldsymbol{\nabla}x^2$ onto $\boldsymbol{\nabla}r$, C_2^2=projection of $\boldsymbol{\nabla}x^2$ onto $\boldsymbol{\nabla}z$, the dot denotes a derivative with respect to ϕ)

$$k_1 = \frac{\sqrt{g}}{r(r^2+\dot{r}^2+\dot{z}^2)^2}\times\{C_2^2[(r^2+\dot{z}^2)\ddot{r} - 2r\dot{r}^2 - r^3 - r\dot{z}^2 - r\dot{z}\ddot{z}] - C_2^1[(\dot{r}^2+r^2)\ddot{z} - \dot{r}\ddot{r}\dot{z} - r\dot{r}\dot{z}]\}. \quad (3)$$

The outcome of this nontrivial exercise is depicted in Fig. 8 for the W7-X configuration, validating the GIST package.

B. Study of the W7-X stellarator

In the following, we will present results from nonlinear ITG simulations, employing adiabatic electrons. Most studies are based on a W7-X equilibrium termed "high-mirror" (hm), but later we also briefly compare with the so-called "low-mirror" (lm) equilibrium (for details about these configurations along with their neoclassical properties, see Ref. 29).

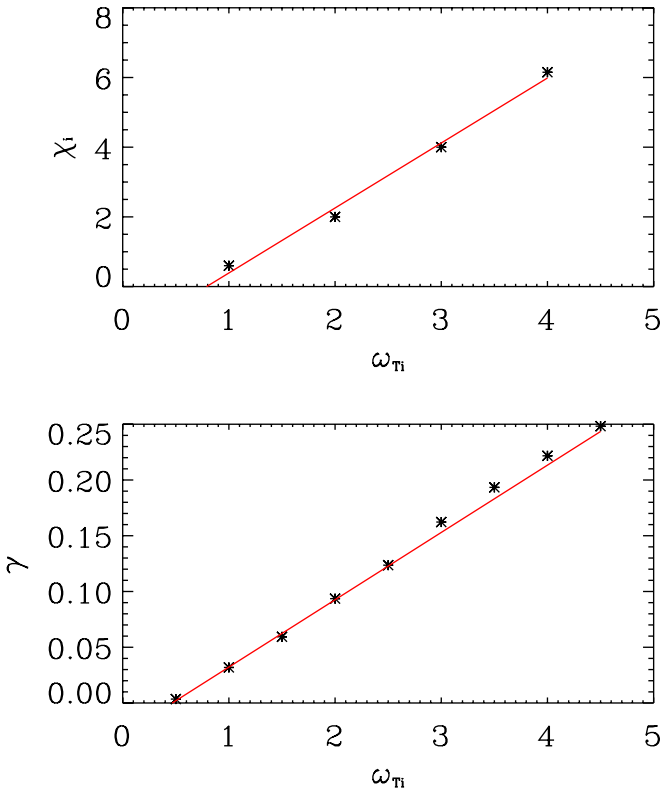

FIG. 9. (Color online) (Top) Ion heat diffusivity χ_i (in units of $\varrho_s^2 c_s/a$) as a function of the ion temperature gradient ω_{T_i}. (Bottom) Linear growth rate γ of the most dominant mode (in units of c_s/a) vs ω_{T_i}.

For all W7-X cases, the flux tubes cross the bean shaped plane at $\theta=0$ and lie on a surface at about 0.7 of the average minor radius. Concerning the resolution of these simulations, extensive convergence tests suggested the following setup: $N_x\times N_y\times N_z=96\times 64\times 128$ grid points are employed in the radial, binormal, and parallel direction, respectively, whereas in velocity space, $N_{v_\parallel}\times N_\mu=48\times 16$ grid points are used.

In Fig. 9, we show a scaling of the anomalous ion heat diffusivity χ_i with respect to the ion temperature gradient $\omega_{T_i}=-(1/T_i)dT_i/dx^1$ (for all cases, the density profile is assumed to be flat and the ion to electron temperature ratio equals unity). In conjunction with the critical gradient derived from the linear growth rates, one can infer the magnitude of the "Dimits shift" (i.e., the nonlinear upshift of the critical gradient), a phenomenon which is attributed to zonal flow activity. In this particular study, we find an upshift of about 35%, which is comparable to tokamak simulation results for adiabatic ITG turbulence in $\hat{s}$-α geometry. The important role of zonal flows in these runs is confirmed by an additional test run (for $\omega_{T_i}=4$), in which we artificially suppress the zonal component of the electrostatic potential (see Fig. 10). It is clearly seen that the level of the ion radial heat flux is increased substantially (although maybe less than in the tokamak case). This result is also in line with Ref. 23, where the selected flux tube was in the proximity of the magnetic axis.

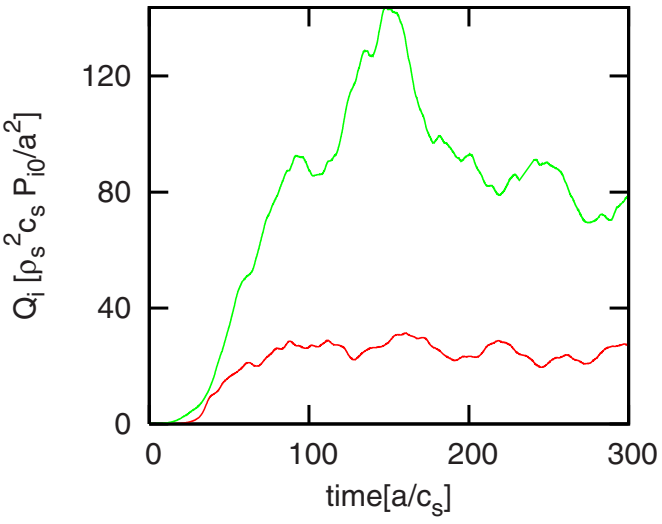

FIG. 10. (Color online) Time traces of the ion heat flux Q_i for the W7-X (hm) configuration. The lower curve depicts the standard simulation, whereas the upper one the simulation with zeroed out zonal flows.

Next, we would like to make some remarks concerning the comparison between the (lm) and (hm) configurations (in reality, these are just two members of a whole sequence of mirror configurations). It is worth pointing out that these two topologies are identical (e.g., they have the same iota profile, metric elements, and curvature components) up to the structure of the magnetic field. A major consequence is that the overlap of the bad curvature regions with the magnetic wells differs. In particular, for the (lm) configuration, all magnetic wells overlap with the bad curvature regions, whereas for the (hm) configuration, a portion of the trapped population around the outboard midplane is displaced towards regions of favorable curvature. Interestingly, as is shown in Fig. 11, the (hm) configuration manifests a lower level of ion heat flux—although the linear properties of the dominant and subdominant microinstabilities are found to be practically the same. Careful numerical resolution tests have confirmed this finding, and zonal flow damping tests point to potential differences in the behavior of geodesic acoustic modes. A detailed analysis, also including kinetic electrons, will appear in a forthcoming work.

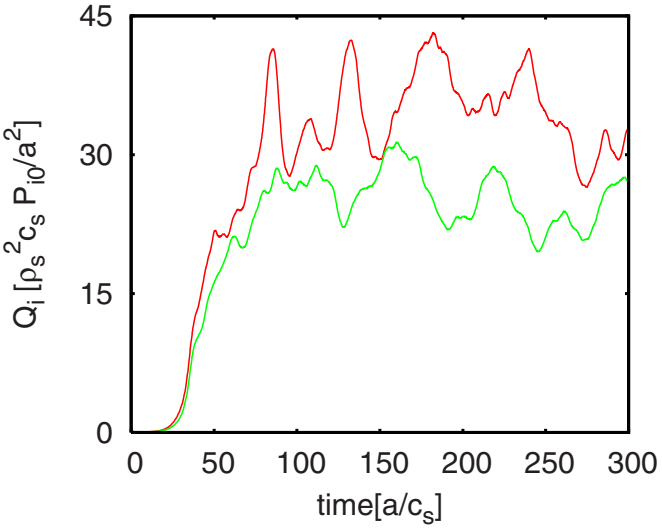

FIG. 11. (Color online) Comparison of the ion heat flux Q_i for the (lm) configuration (upper line) and for the (hm) configuration (lower line).

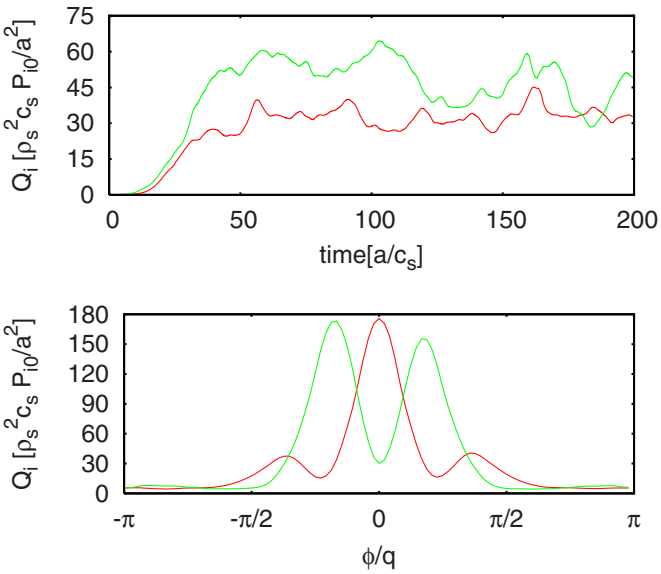

FIG. 12. (Color online) (Top) Time traces of the ion heat flux Q_i for the banana tube (lower line) and the bullet tube (upper line). (Bottom) Parallel mode structure of the same quantity for both tubes.

C. Study of the NCSX stellarator

In this subsection, we provide results from nonlinear ITG simulations with adiabatic electrons—using the same resolution as for W7-X—for the quasiaxisymmetric optimization scenario as implemented in the NCSX stellarator. As mentioned before, nonaxisymmetry results in the fact that different flux tubes on the same flux surface may not be equivalent with respect to their turbulent properties. This is demonstrated in Fig. 12, where we compare the radial ion heat fluxes in terms of level and parallel mode structure for two flux tubes. In the first case, the tube crosses the banana plane at $\theta=0$, and in the second, it crosses the bullet plane at $\theta=0$ (in addition, $\omega_{T_i}=4$, and the density profile is flat). It is shown that there exists a difference in the levels of the order of 35%, together with a pronounced disparity in the parallel mode structure. More specifically, the "banana" tube behaves much like a typical tokamak since the mode peaks at the outer midplane and there is a strong fall off towards the ends of the tube. In contrast to this, the "bullet" tube manifests two distinct peaks off the outboard midplane.

Interestingly, if one compares the ion heat diffusivities (in units of $\varrho_s^2 c_s / L_{T_i}$) at several times the linear threshold (which is the case here) with the respective values obtained for cyclone base case tokamak simulations, one finds that they are very similar. However, the flux-gradient relationships are quite different in these two scenarios, as it turns out. While in the tokamak case, the ion heat flux is offset-linear in the normalized gradient, here it is the respective diffusivity. This means that closer to criticality, but at the same relative distance from the linear threshold, the heat flux

will be lower in the NCSX geometry. Moreover, since different flux tubes on the same magnetic surface have different onset conditions, there will be a softening of the threshold. These two effects might allow the stellarator plasma to deviate more substantially from the linear thresholds than in a tokamak. Future gyrokinetic work will have to test these ideas in full flux surface and full torus simulations.

IV. SUMMARY AND CONCLUSIONS

In this paper, we have presented linear and nonlinear gyrokinetic simulations with the GENE code for tokamak edge plasmas as well as for stellarator core plasmas, shedding light on the behavior of plasma microturbulence under near-separatrix or nonaxisymmetric conditions. To this aim, the required geometric coefficients were inferred directly from the respective MHD equilibria via the GIST code.

For ASDEX Upgrade edge plasmas, linear simulations show the existence of ETG instabilities which become unstable for $\eta_e \gtrsim \eta_{e,\mathrm{crit}} \approx 1.2$. In the edge, taking into account effects from strong shaping and up-down asymmetry, certain characteristics of this instability deviate from the known core ETG behavior. Most prominently, one finds that the largest linear growth rates are not at zero radial wavenumber, but at some finite value, forcing one to produce two-dimensional wavenumber spectra. This behavior can be understood by means of the properties of local shear, which is—although global shear is positive almost everywhere—strongly negative on the outboard side. In nonlinear simulations, on the other hand, the modes which peak at the outboard midplane (zero radial wavenumber) prevail; transport then peaks at very small scales in the range of $k_\perp \varrho_s \approx 15$. The electron heat diffusivities obtained in these simulations are quite close to the experimentally measured ones. While our simulations cannot—and do not attempt to—make a statement about the causes of the *L-H* transition, the ETG instability found in our simulations is a candidate for explaining the residual electron heat transport in the edge. This is supported by the fact that experimentally measured η_e values are of the order of two in normal *H*-modes, which is well within the unstable ETG regime discussed here.

Concerning stellarator devices, we reported on the recently developed code GIST for the construction of the geometric input data for GENE. This integrated package can read in output files from VMEC equilibria and combines, in a consistent manner, the MHD approach with 3D field-line tracing. This powerful feature was first applied to the optimized stellarator Wendelstein 7-X. Here, it was shown that for the case we considered, adiabatic ITG turbulence has characteristics which resemble those in the tokamak core. In particular, zonal flows were identified as the dominant saturation mechanism, and the simulations exhibited a significant Dimits shift. Moreover, subtle geometric differences between two very similar configurations lead to substantial differences in the resulting ion heat flux, although the linear properties of the underlying microinstabilities are virtually invariant. Further investigations along these lines will be published elsewhere. Finally, adiabatic ITG turbulence simulations with GENE for the quasiaxisymmetric stellarator NCSX were performed, showing that two different flux tubes on the same magnetic surface may yield a substantial but still moderate difference of a few 10% in the transport levels. Due to qualitative differences in the flux-gradient relationships, the near-threshold heat flux is lower in the NCSX geometry than in a circular tokamak. Moreover, since different flux tubes on the same magnetic surface have different onset conditions, there will be a softening of the threshold. Both effects might allow the stellarator plasma to deviate more substantially from the linear thresholds than in a tokamak. These findings point to a significant potential for a systematic optimization of turbulent transport in stellarators which will have to be explored in more detail in the future.

ACKNOWLEDGMENTS

The authors wish to thank T. Görler for help with the GENE code, A. Boozer, G. Conway, D. Coster, G. Hammett, and E. Wolfrum for valuable discussions, W. Cooper and Yu. Turkin for useful contributions to the GIST package, and J. Geiger for providing data from VMEC.

[1] J. W. Connor, R. J. Hastie, and J. B. Taylor, Phys. Rev. Lett. **40**, 396 (1978).
[2] R. L. Miller, M. S. Chu, J. M. Greene, Y. R. Lin-Liu, and R. E. Waltz, Phys. Plasmas **5**, 973 (1998).
[3] T.-H. Watanabe, H. Sugama, and S. Ferrando-Margalet, Nucl. Fusion **47**, 1383 (2007).
[4] F. Jenko, W. Dorland, M. Kotschenreuther, and B. N. Rogers, Phys. Plasmas **7**, 1904 (2000).
[5] T. Dannert and F. Jenko, Phys. Plasmas **12**, 072309 (2005).
[6] F. Merz, Ph.D. thesis, University of Münster, 2008.
[7] O. Gruber, H.-S. Bosch, S. Günter, A. Herrmann, A. Kallenbach, M. Kaufmann, K. Krieger, K. Lackner, V. Mertens, R. Neu, F. Ryter, J. Schweinzer, A. Stäbler, W. Suttrop, R. Wolf, K. Asmussen, A. Bard, G. Becker, K. Behler, K. Behringer, A. Bergmann, M. Bessenrodt-Weberpals, K. Borrass, B. Braams, M. Brambilla, R. Brandenburg, F. Braun, H. Brinkschulte, R. Brückner, B. Brüsehaber, K. Büchl, A. Buhler, H. P. Callaghan, A. Carlson, D. P. Coster, L. Cupido, S. de Pena Hempel, C. Dorn, R. Drube, R. Dux, S. Egorov, W. Engelhardt, H.-U. Fahrbach, U. Fantz, H.-U. Feist, P. Franzen, J. C. Fuchs, G. Fussmann, J. Gafert, G. Gantenbein, O. Gehre, A. Geier, J. Gernhardt, E. Gubanka, A. Gude, G. Haas, K. Hallatschek, D. Hartmann, B. Heinemann, G. Herppich, W. Herrmann, F. Hofmeister, E. Holzhauer, D. Jacobi, M. Kakoulidis, N. Karakatsanis, O. Kardaun, A. Khutoretski, H. Kollotzek, S. Kötterl, W. Kraus, B. Kurzan, G. Kyriakakis, P. T. Lang, R. S. Lang, M. Laux, L. L. Lengyel, F. Leuterer, A. Lorenz, H. Maier, M. Manso, M. Maraschek, M. Markoulaki, K.-F. Mast, P. J. McCarthy, D. Meisel, H. Meister, R. Merkel, J. P. Meskat, H. W. Müller, M. Münich, H. Murmann, B. Napiontek, G. Neu, J. Neuhauser, M. Niethammer, J.-M. Noterdaeme, G. Pautasso, A. G. Peeters, G. Pereverzev, S. Pinches, G. Raupp, K. Reinmüller, R. Riedl, V. Rohde, H. Röhr, J. Roth, H. Salzmann, W. Sandmann, H.-B. Schilling, D. Schlögl, K. Schmidtmann, H. Schneider, R. Schneider, W. Schneider, G. Schramm, S. Schweizer, R. R. Schwörer, B. D. Scott, U. Seidel, F. Serra, S. Sesnic, C. Sihler, A. Silva, E. Speth, K.-H. Steuer, J. Stober, B. Streibl, A. Thoma, W. Treutterer, M. Troppmann, N. Tsois, W. Ullrich, M. Ulrich, P. Varela, H. Verbeek, O. Vollmer, H. Wedler, M. Weinlich, U. Wenzel, F. Wesner, R. Wunderlich, N. Xantopoulos, Q. Yu, D. Zasche, T. Zehetbauer, H.-P. Zehrfeld, H. Zohm, and M. Zouhar, Nucl. Fusion **39**, 1321 (1999).
[8] G. H. Neilson, A. H. Reiman, M. C. Zarnstorff, A. Brooks, G.-Y. Fu, R. J. Goldston, L.-P. Ku, Z. Lin, R. Majeski, D. A. Monticello, H. Mynick, N. Pomphrey, M. H. Redi, W. T. Reiersen, J. A. Schmidt, S. P. Hirshman, J. F. Lyon, L. A. Berry, B. E. Nelson, R. Sanchez, D. A. Spong, A. H. Boozer, W. H. Miner, Jr., P. M. Valanju, W. A. Cooper, M. Drevlak, P. Merkel, and C. Nuehrenberg, Phys. Plasmas **7**, 1911 (2000).
[9] G. Grieger, C. D. Beidler, H. Maassberg, E. Harmeyer, F. Herrnegger, J. Junker, J. Kisslinger, W. Lotz, P. Merkel, J. Nührenberg, F. Rau, J. Sapper, A. Schlüter, F. Sardei, and H. Wobig, *Plasma Physics and Controlled*

Nuclear Fusion Research 1990 (International Atomic Energy Agency, Vienna, 1991), Vol. 3, p. 525.
[10]M. Kammerer, F. Merz, and F. Jenko, Phys. Plasmas **15**, 052102 (2008).
[11]P. Xanthopoulos and F. Jenko, Phys. Plasmas **13**, 092301 (2006).
[12]D. Told, F. Jenko, P. Xanthopoulos, L. D. Horton, and E. Wolfrum, and the ASDEX Upgrade Team, Phys. Plasmas **15**, 102306 (2008).
[13]R. J. Groebner and T. H. Osborne, Phys. Plasmas **5**, 1800 (1998).
[14]R. E. Waltz, G. D. Kerbel, and J. Milovich, Phys. Plasmas **1**, 2229 (1994).
[15]F. Jenko, J. Plasma Fusion Res. **6**, 11 (2004).
[16]F. Jenko, W. Dorland, and G. W. Hammett, Phys. Plasmas **8**, 4096 (2001).
[17]L. D. Horton, A. V. Chankin, Y. P. Chen, G. D. Conway, D. P. Coster, T. Eich, E. Kaveeva, C. Konz, B. Kurzan, J. Neuhauser, I. Nunes, M. Reich, V. Rozhansky, S. Saarelma, J. Schirmer, J. Schweinzer, S. Voskoboynikov, and E. Wolfrum, and the ASDEX Upgrade Team, Nucl. Fusion **45**, 856 (2005).
[18]D. P. Coster, X. Bonnin, A. V. Chankin, H.-J. Klingshirn, C. Konz, G. Pautasso, M. Wischmeier, E. Wolfrum, and the ASDEX Upgrade Team, Proceedings of 22nd International Conference, Geneva, IAEA, 2008, Paper No. TH/P4-3.
[19]P. Xanthopoulos, D. Mikkelsen, F. Jenko, W. Dorland, and O. Kalentev, Phys. Plasmas **15**, 122108 (2008).
[20]T. M. Antonsen, Jr., J. F. Drake, P. N. Guzdar, A. B. Hassam, Y. T. Lau, C. S. Liu, and S. V. Novakovskii, Phys. Plasmas **3**, 2221 (1996).
[21]F. Jenko and A. Kendl, New J. Phys. **4**, 35 (2002).
[22]F. Jenko and A. Kendl, Phys. Plasmas **9**, 4103 (2002).
[23]P. Xanthopoulos, F. Merz, T. Görler, and F. Jenko, Phys. Rev. Lett. **99**, 035002 (2007).
[24]T.-H. Watanabe, H. Sugama, and S. Ferrando-Margalet, Phys. Rev. Lett. **100**, 195002 (2008).
[25]D. V. Anderson, W. A. Cooper, R. Gruber, S. Merazzi, and U. Schwenn, Int. J. Supercomput. Appl. **4**, 34 (1990).
[26]W. A. Cooper, Plasma Phys. Controlled Fusion **34**, 1011 (1992).
[27]S. P. Hirshman and D. K. Lee, Comput. Phys. Commun. **39**, 161 (1986).
[28]J. Nührenberg and R. Zille, *Theory of Fusion Plasmas* (Editrice Compositori, Bologna, 1988).
[29]C. D. Beidler and H. Maassberg, Plasma Phys. Controlled Fusion **43**, 1131 (2001).